Statistical approach for detection and localization of a fluorescing mouse tumor in Intralipid

Adam B. Milstein, Michael D. Kennedy, Philip S. Low, Charles A. Bouman, and Kevin J. Webb

We present a method for detecting and localizing a fluorescing tumor obscured underneath several millimeters of a multiply scattering, homogeneous medium from fluorescence measurements made above the surface. Using a statistical model of the measurement system, we develop approaches for detection by use of a binary hypothesis testing approach and localization by use of maximum-likelihood estimation. We also compute the probability of tumor detection and the Cramér–Rao lower bound for the localization estimate error, which are performance metrics that could potentially be optimized in an experimental design. We validate the methods in an experimental study involving an excised mouse tumor tagged with a new folate-indocyanine dye and obscured under a tissue-simulating lipid suspension.

OCIS codes: 170.6280, 290.7050, 100.3010, 100.3190, 100.6950, 170.3010.

1. Introduction

Currently, the only assured cure for the vast majority of cancers involves the complete resection of all malignant lesions. Achievement of this objective, however, is often limited by the inability of the surgeon to identify and localize all cancerous tissues. In some cases, neoplastic loci are difficult to distinguish from adjacent normal tissue. In other situations, they are not detected by the surgeon because of their small size or obscured location. Even after removal of visible tumor masses during surgical debulking, microscopic tumors not visible to the naked eye can often be the source of recurrent disease.[1]

Recent advances in biomedical optical imaging based on fluorescent dyes[2] offer great promise in diagnosing malignant tissue, monitoring tumor therapy progress, and guiding surgical intervention for tumor removal. Optical imaging is safe and relatively inexpensive compared with other modalities, and optical measurement probes have the potential to be small, maneuverable, and unobtrusive. These properties can be particularly attractive in an intraoperative environment where real-time imaging may be required over a period of hours.

Fluorescence optical diffusion tomography (FODT), in which full volumetric images of fluorescence are reconstructed from measurements on the boundary, has generated considerable interest.[3–9] However, although FODT offers the advantage of quantitative imaging, it is an ill-posed inverse problem that is often computationally demanding. This has motivated interest in simpler, more computationally efficient approaches that localize fluorophores in a turbid medium, but fall short of quantitative FODT. Previously, the problem of localizing fluorophores in real animal tissue, tissue-simulating phantoms, or computational simulations has been considered in a variety of studies. Chen *et al.*[10] have used a near-infrared (near-IR) measurement system with dual interfering sources to determine the two-dimensional (2-D) location of a fluorescing tumor in a mouse subject. The mouse was injected with a contrast agent that selectively targeted the tumor because of its increased metabolic activity. Gannot *et al.*[11] performed a three-dimensional (3-D) localization of a targeted fluorophore in the tongue of live mouse subjects underneath 1–2-mm Intralipid–agarose slabs. The authors measured surface fluorescence with a camera, and they used a Levenburg–Marquardt method in their localization procedure to fit the data to a random-walk model. Hull *et al.*[12] have accurately de-

A. B. Milstein (milstein@ll.mit.edu), C. A. Bouman, and K. J. Webb are with the School of Electrical and Computer Engineering, Purdue University, 465 Northwestern Avenue, West Lafayette, Indiana 47907-2035. M. D. Kennedy and P. S. Low are with the School of Chemistry, Purdue University, West Lafayette, Indiana 47907-2084.

Received 30 July 2004; revised manuscript received 21 November 2004; accepted 23 November 2004.

0003-6935/05/122300-11$15.00/0

termined the depth of a small fluorescent sphere embedded within a turbid medium by use of fluorescence measurements on the surface. The sample was illuminated from the side with an expanded laser beam, and the fluorescence was collected from the top surface with a linear array of detector fibers. Pfister and Scholz[13] have used a multiple-signal classification algorithm to localize fluorescent spots under tissuelike scatter in a computational simulation. All the localization approaches essentially perform a fit between measured data and theory. To date, the question of how to compute the probability of tumor detection, or how to obtain theoretical precision bounds for the localization, has not been addressed to our knowledge.

Recently, several advancements have been made in the development of fluorescent contrast agents that specifically target cancer cells. Receptors for the vitamin folic acid are expressed at high levels in a number of tumor types including ovarian,[14] breast,[15] brain,[16] kidney,[17] lung,[18] uterine,[15] and others. In nonmalignant tissues, expression of folate receptors (FRs) is found only in a few tissue types.[19–21] Because of the rare occurrence of FRs in normal tissues and their high level of expression in tumors, FRs are a strong candidate for obtaining tumor targeting with little uptake into normal tissues. FR targeting has previously been used for radioimaging, magnetic resonance imaging, and optical imaging.[22–25] Optical imaging agents targeted with folate have been developed with near-IR dyes as well as visible dyes,[24,25] resulting in high tumor-to-background contrast.

Here we use a statistical model of the measurement system to develop approaches for detection by use of a binary hypothesis testing approach and localization by use of a maximum-likelihood (ML) estimation. For the detection problem, we provide expressions for the tumor's detection probability. We also compute the Cramér–Rao lower bound for the localization error. These bounds allow one to predict the performance and solvability of a detection and localization problem in advance, before making measurements, and hence can be used to optimize an experimental design. Previously, the Cramér–Rao bound was computed in other inverse scattering applications to bound the localization error[26] and to compute performance limits in parametric, shape-based imaging.[27,28] In addition, hypothesis testing has been explored for linearized inverse scattering problems.[29] We apply these to the problem of detecting and localizing a fluorescent tumor.

We validate the methods in an experimental study using an excised mouse tumor tagged with a new folate-indocyanine dye and obscured under a tissue-simulating lipid suspension. The new targeted folate-indocyanine dye was designed to operate with excitation at 785 nm, a common wavelength for inexpensive diode lasers and a useful one for biomedical optics due to tissue's relatively low absorption.[30,31] The dye was injected into a mouse, where it accumulated preferentially in a lung tumor. The mouse tumor was then excised and placed into a tissue-simulating Intralipid–agarose gel phantom. Use of an excised real mouse tumor in the Intralipid suspension, instead of just the dye molecules, ensures that a medically realistic dose of the drug has been used in the experiment. Hence, the fluorescence signature resulting from the tumor is one that could conceivably be encountered in a clinical application. We used a fluorescence microscope to perform a one-dimensional (1-D) measurement scan. From these data, we estimated the tumor's lateral and depth coordinates and instrument model parameters, which we subsequently used to compute the performance bounds.

2. Models

A. Coupled Diffusion Equations

Here we briefly review the diffusion equation description of light in multiply scattering media such as tissue.[3,4] In applications where scattering dominates over absorption, the transport of light modulated at angular frequency ω through a scattering medium can be modeled with the photon diffusion equation.[32,33] For the $\exp(j\omega t)$ time variation, the diffusion equation is given by

$$\nabla \cdot [D(\mathbf{r}) \nabla \phi(\mathbf{r}, \omega)] - [\mu_a(\mathbf{r}) + j\omega/c]\phi(\mathbf{r}, \omega) = -\delta(\mathbf{r} - \mathbf{r}_{s_i}), \quad (1)$$

where $\phi(\mathbf{r}, \omega)$ ($\mathrm{W/cm^2}$) is the complex modulation envelope of the photon fluence rate, $\mathbf{r}_{s_i}$ is the point-source location, and $\delta(\mathbf{r})$ is the Dirac function. The diffusion coefficient $D(\mathbf{r})$ (cm) is inversely related to the reduced scattering coefficient, and $\mu_a(\mathbf{r})$ ($\mathrm{cm^{-1}}$) is the absorption coefficient. Note that we assume that the laser excitation can be modeled as an isotropic point source at position $\mathbf{r}_{s_i}$.

For the case in which the scattering medium contains a fluorophore, the fluorophore is excited with light at wavelength λ_x and emits light at a longer wavelength λ_m. We use two coupled diffusion equations to describe a fluorescence measurement, with the first to represent λ_x excitation and the second to represent the emitted λ_m photons[34–36]:

$$\nabla \cdot [D_x(\mathbf{r}) \nabla \phi_x(\mathbf{r}, \omega)] - [\mu_{a_x}(\mathbf{r}) + j\omega/c]\phi_x(\mathbf{r}, \omega) = -\delta(\mathbf{r} - \mathbf{r}_{s_i}), \quad (2)$$

$$\nabla \cdot [D_m(\mathbf{r}) \nabla \phi_m(\mathbf{r}, \omega)] - [\mu_{a_m}(\mathbf{r}) + j\omega/c]\phi_m(\mathbf{r}, \omega) = -\phi_x(\mathbf{r}, \omega)\eta\mu_{a_f}(\mathbf{r}) \frac{1 - j\omega\tau(\mathbf{r})}{1 + [\omega\tau(\mathbf{r})]^2}, \quad (3)$$

where the subscripts x and m denote excitation and emission wavelengths λ_x and λ_m, respectively. The fluorescent lifetime $\tau(\mathbf{r})$ (s) is the fluorophore's characteristic exponential decay constant. The fluorescent yield $\eta\mu_{a_f}(\mathbf{r})$ ($\mathrm{cm^{-1}}$) incorporates the fluorophore's quantum efficiency η and its absorption coefficient μ_{a_f}.

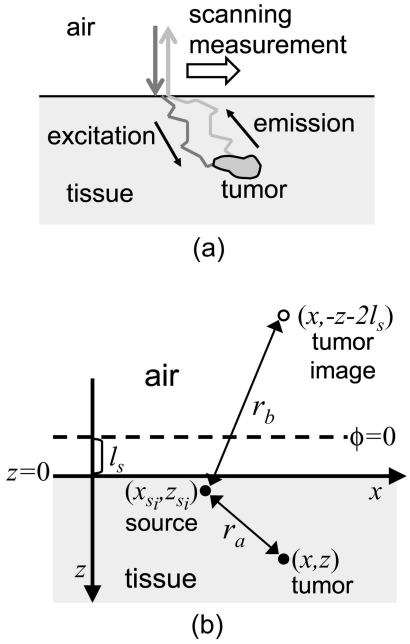

Fig. 1. (a) Illustration of a fluorescence scan measurement, with photons migrating within the scattering tissue. (b) Semi-infinite geometry used to derive the forward model. The method of images is used to ensure that $\phi = 0$ for the boundary at a distance of l_s outside of the physical air–tissue interface.

B. Forward Model

Consider a fluorescence measurement scan, where a single source–detector position is scanned over the top of a tissue surface to probe for a fluorescing submerged tumor. Figure 1(a) illustrates this measurement, with photons migrating from the source position to the tumor and emitted photons migrating back to the same position. The inverse problem is to determine the tumor's position from the fluorescence measurements. We use a forward model based on Eq. (1) that gives the expected measurements that would result from a tumor at a known position.

For simplicity, we impose a few restrictions, although most of these are straightforward to remove. We consider only the $\omega = 0$ case, where unmodulated light is used, and we assume that $\mu_{a_x} = \mu_{a_m}$ and $D_x = D_m$, so that the diffusion equation Green's functions are the same for λ_x and λ_m. We also model the tumor as a point fluorophore, and we examine the validity of this approximation in Subsection 2.C. Finally, we model the tissue as a semi-infinite region with homogeneous μ_a and D so that a closed-form analytical solution to the diffusion equation can be employed. This model allows for a rapid solution to the localization inverse problem.

Let $\mathbf{y}$ denote the measurement vector and let $\tilde{\mathbf{f}}(\mathbf{r})$ denote the fluorescence data vector expected from the diffusion model due to a point fluorophore at location $\mathbf{r}$. We assume a source wavelength of λ_x and a detector wavelength of λ_m. Let the measurement source positions be identified as $\mathbf{r}_{s_i}$ and let the tumor centroid position be denoted by $\mathbf{r}$. In addition, let $g(\mathbf{r}_{s_i}, \mathbf{r})$ denote the domain's Green's function obtained as the solution to Eq. (1), with the source at $\mathbf{r}_{s_i}$ and the observation at $\mathbf{r}$. We also denote the recorded measurement at $\mathbf{r}_{s_i}$ as y_i. Using the coupled diffusion equations of Eqs. (2) and (4) and the approximations noted above, we can give the fluorescence recorded at $\mathbf{r}_{s_i}$ from a point fluorophore located at $\mathbf{r}$ by $\tilde{f}_i(\mathbf{r}) = g(\mathbf{r}_{s_i}, \mathbf{r})g(\mathbf{r}, \mathbf{r}_{s_i})w_0$, where the first Green's function represents the excitation light reaching the tumor, the second represents the light emitted by the tumor back to the measurement point, and w_0 is a constant that incorporates the tumor's $\eta\mu_{a_f}$ and the efficiency of light coupling into the medium. Using the reciprocity theorem,[37] we can interchange the source and observation positions of the Green's function, and $\tilde{f}_i(\mathbf{r}) = [g(\mathbf{r}_{s_i}, \mathbf{r})]^2 w_0$.

Suppose the air–tissue interface is located at $z = 0$ and that the region $z > 0$ consists of tissue. We use the extrapolated zero-flux boundary condition for the diffusion equation, where the extrapolation distance $l_s = 5.03D$ is chosen to model a scattering domain interface where the scatterers are assumed to be in water with a refractive index of 1.33.[38] We apply the method of images to enforce the $\phi(z = -l_s) = 0$ boundary condition, as shown in Fig. 1(b). The excitation source is modeled as an effective isotropic point source located one transport length inside the medium at $z_{s_i} = 3D$.[38] We assume a semi-infinite, homogeneous medium, with a point fluorophore at $\mathbf{r} = (x, y, z)$ and the measurement position at $\mathbf{r}_{s_i} = (x_{s_i}, y, z_{s_i})$. We define

$$r_a = [(x - x_{s_i})^2 + (z - z_{s_i})^2]^{1/2}, \tag{4}$$

$$r_b = [(x - x_{s_i})^2 + (z + z_{s_i} + 2l_s)^2]^{1/2}. \tag{5}$$

The forward model is given by[38]

$$\tilde{f}_i(\mathbf{r}) = \left[\frac{\exp(-kr_a)}{r_a} - \frac{\exp(-kr_b)}{r_b}\right]^2 w, \tag{6}$$

$$= f_i(\mathbf{r})w, \tag{7}$$

where we bundled the multiplicative constants from the closed-form Green's function and w_0 into a new parameter w, $k = \sqrt{\mu_a/D}$, and the definition of f_i is implied. Note that we consider a 2-D geometry, where the laser excitation and the tumor are located at the same y position, so no y terms appear in Eq. (6).

C. Validity of Point Tumor Source Model

In Subsection 2.B we assumed that a fluorescing tumor can be approximated as a single point. To investigate the validity of this assumption for scan measurements similar to the one in our experiment, we performed a numerical simulation study with a fluorophore dispersed throughout a spherical domain of varying size and depth.[39] The 3 cm $\times$ 3 cm $\times$ 3 cm tissue phantom of Fig. 2(a) with homogeneous background $\mu_a = 0.03\ \text{cm}^{-1}$ and $D = 0.033$ cm was

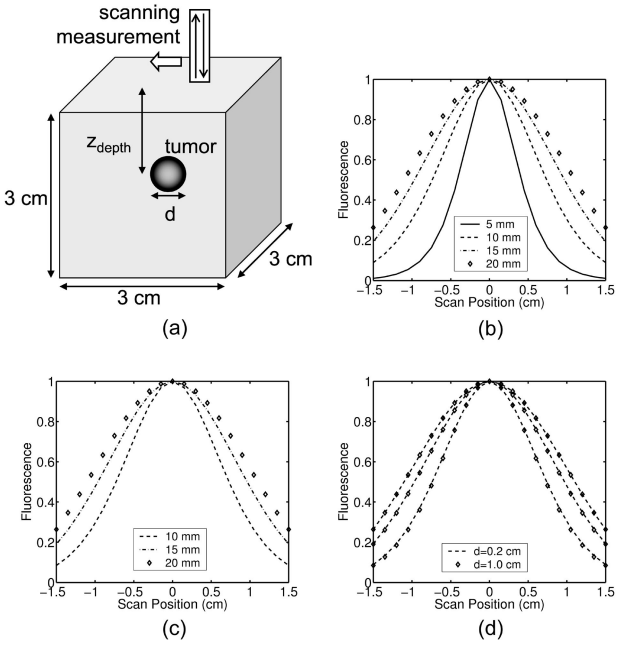

Fig. 2. Simulated measurement of a tumor of diameter d at depth z_{depth}, with all data sets normalized to the maximum value. (a) Geometry. (b) Plot of simulated normalized intensity profile for a small tumor at different depths, with $d = 2$ mm. (c) Plot of the intensity profile for a large tumor at different depths, with $d = 1.0$ cm. (d) Superimposed plots from two different-sized tumors, showing the relative invariance to size.

considered. Two different-sized tumors were considered: a 2-mm fluorescent sphere and a 1-cm sphere. Each had $\eta\mu_{a_f} = 0.02\ \text{cm}^{-1}$, $\mu_a = 0.030\ \text{cm}^{-1}$, and the same scattering properties as the background. A 1-D scan (with unmodulated light) across the top of the surface over the tumor was simulated, assuming a conceptual instrument containing a source and detector in the same position. The region was discretized into $65 \times 65 \times 65$ voxels, and 21 measurements were simulated with multigrid finite differences to solve the diffusion equation. The simulation used a numerical code that we previously compared favorably with experimental data,[3,4] leading us to a high degree of confidence in the precision of the numerical simulations. Figure 2(b) shows the simulated measurements of fluorescence for the small tumor at four different depths. The scans are normalized to the maximum because the signal from the larger tumor was greater. Figure 2(c) shows the simulated measurements of fluorescence for the large tumor at three different depths. Figure 2(d) superimposes the two results. Note in Fig. 2(d) that the measured intensity profile is relatively invariant to the tumor's size, giving similar results as a function of tumor depth for the two different tumor sizes considered. This result suggests that a simple point tumor model is sufficiently accurate for localizing the centroid of a tumor in a similar 1-D scanning experiment. We note, however, that this observation may not apply to other measurement geometries.

D. Detector Noise Model

For the detector noise, we assume the same shot-noise model presented previously by Ye *et al.*[40] Let $\mathbf{y}$ denote the vector of measurements and $\mathbf{n}$ denote the corresponding detector noise vector. We assume that $\mathbf{n}$ is independent, zero mean, and Gaussian with the covariance given by Υ, where

$$[\Upsilon]_{ii} = \alpha\,|\,y_i\,|\,, \tag{8}$$

and α is a scalar parameter of the measurement system. Previously, Ye *et al.*[41] presented a method for estimating α from the measured data while solving the optical diffusion tomography inverse problem. In Section 5 we apply this estimation method to obtain the value of α that we use to compute statistical performance bounds related to our experimental study.

3. Detection

Here we describe a procedure for detecting the presence of a tumor, and we compute the probability of detecting a tumor for a specified false-alarm rate. As we demonstrate in Subsection 5.D, the probability of detection can be plotted as a function of tumor position for a particular measurement system, allowing one to characterize the instrument's diagnostic capabilities. The detection problem can be viewed as a binary hypothesis testing problem.[42] Let hypothesis H_0 correspond to the absence of a tumor, and let the composite hypothesis $H_{1,\theta}$ correspond to the presence of a tumor parameterized by the vector $\theta = [x \quad z \quad w]^T$, where x and z give the location and w incorporates all scalar factors in the measurement. Let $\mathbf{y}$ denote the measurement vector of length P, and let $\mathbf{n}$ be the independent Gaussian noise vector with covariance Υ introduced in Subsection 2.D. The densities for $\mathbf{y}$ under both hypotheses are given by

$$p_0(\mathbf{y}) = \frac{1}{[(2\pi)^P\,|\,\Upsilon\,|\,]^{1/2}} \exp\left(-\frac{1}{2}\,\|\mathbf{y}\|^2_{\Upsilon^{-1}}\right), \tag{9}$$

$$p_{1,\theta}(\mathbf{y}) = \frac{1}{[(2\pi)^P|\Upsilon|]^{1/2}} \exp\left[-\frac{1}{2}\,\|\mathbf{y} - w\mathbf{f}(\mathbf{r})\|^2_{\Upsilon^{-1}}\right], \tag{10}$$

where $\mathbf{r} = [x \quad z]^T$, and $\|\mathbf{u}\|_{\mathbf{v}}^2 = \mathbf{u}^H\mathbf{V}\mathbf{u}$.

Suppose for the moment that θ is known, and let P_F be the false-alarm rate that one wishes to achieve. The Neyman–Pearson lemma[42] indicates that a likelihood ratio test (LRT) produces the highest probability of detection for a specified false-alarm rate of P_F. We form the log likelihood ratio $L(\mathbf{y}, \theta) = \ln p_{1,\theta}(\mathbf{y})/p_0(\mathbf{y})$, compare it with a threshold $\tilde{k}_{P_F}(\theta)$ (which is determined by P_F), and declare a tumor present if $L(\mathbf{y}, \theta) > \tilde{k}_{P_F}(\theta)$.

By writing out the ratio of Eqs. (10) and (9) and taking the logarithm, we obtain

$$L(\mathbf{y},\ \theta) = \mathbf{h}^T(\theta)\mathbf{y} - c(\theta), \tag{11}$$

where $\mathbf{h}^T(\theta) = w\mathbf{f}^T(\mathbf{r})\mathbf{\Upsilon}^{-1}$, $c(\theta) = \frac{1}{2}w^2\mathbf{f}^T(\mathbf{r})\mathbf{\Upsilon}^{-1}\mathbf{f}(\mathbf{r})$. Hence the LRT is equivalent to comparing $q = \mathbf{h}^T(\theta)\mathbf{y}$ with a threshold, which we call $k_{P_F}(\theta)$. Note that the LRT is similar to matched filtering, as we evaluate a cross correlation between the data $\mathbf{y}$ and the forward model $\mathbf{f}(\mathbf{r})$ and compare it with a threshold.

We can determine the threshold $k_{P_F}(\theta)$ by rewriting the LRT in a more revealing form, using $q = \mathbf{h}^T(\theta)\mathbf{y}$ rather than $\mathbf{y}$. We obtain the 1-D Gaussian distributions $p_0(q)$ and $p_{1,\theta}(q)$ by computing the required moments:

$$E_0(q) = \mathbf{h}^T(\theta)E_0(\mathbf{y}) \tag{12}$$

$$= 0, \tag{13}$$

$$E_{1,\theta}(q) = E_{1,\theta}[\mathbf{h}^T(\theta)\mathbf{y}]$$

$$= w^2\mathbf{f}^T(\theta)\mathbf{\Upsilon}^{-1}\mathbf{f}(\theta), \tag{14}$$

$$\sigma_q^{\ 2} = E_0[\mathbf{h}^T(\theta)\mathbf{n}\mathbf{n}^T\mathbf{h}(\theta)] \tag{15}$$

$$= \mathbf{h}^T(\theta)\mathbf{\Upsilon}\mathbf{h}(\theta). \tag{16}$$

By definition, the false-alarm rate P_F is given by

$$P_F = \int_{k_{P_F}}^{\infty} p_0(q)\mathrm{d}q = 1 - \mathrm{erf}_*\left(\frac{k_{P_F}}{\sigma_q}\right), \tag{17}$$

where we define

$$\mathrm{erf}_*(r) = \int_{-\infty}^{r} \frac{1}{\sqrt{2\pi}} \exp\left(-\frac{1}{2}t^2\right)\mathrm{d}t. \tag{18}$$

Hence the threshold k_{P_F} that allows us to achieve a false-alarm rate P_F is

$$k_{P_F} = \sigma_q\, \mathrm{erf}_*^{-1}(1 - P_F). \tag{18'}$$

To assess the achievable performance of the tumor detection approach, we compute the probability of a successful tumor detection. The receiver operating characteristic (ROC)[42] is defined as the probability of detection $P_D(P_F)$ specified as a function of the false-alarm rate P_F. Using the threshold k_{P_F} computed in Eq. (18'), we obtain

$$P_D = \int_{k_{P_F}}^{\infty} p_{1,\theta}(q)\mathrm{d}q \tag{19}$$

$$= 1 - \mathrm{erf}_*\left(\frac{k_{P_F} - \bar{q}}{\sigma_q}\right) \tag{20}$$

$$= 1 - \mathrm{erf}_*\left[\mathrm{erf}_*^{-1}(1 - P_F) - \frac{\bar{q}}{\sigma_q}\right], \tag{21}$$

where $\bar{q} = E_{1,\theta}(q)$. From Eq. (21), the ROC is specified for every value of θ (thus for any possible tumor location).

In practice, the tumor position and the true value of w are not known. Because the LRT assumes a known θ, we must use a modification of the LRT called the generalized likelihood ratio test (GLRT).[42] In the GLRT, we first suppose that the tumor is present, and we compute the ML estimate $\hat{\theta} = \arg\max_\theta p_{1,\theta}(\mathbf{y})$. We then perform the LRT, using $\hat{\theta}$ in place of θ. Because the GLRT must be used, the ROC specified in Eq. (21) cannot be achieved in practice and must be considered an upper bound for the true probability of detection.[42] Computing the ML estimate $\hat{\theta}$ is the problem of localization, which is addressed in Section 4.

4. Localization

If a tumor is present, we wish to localize it by estimating its x and z coordinates. In the process, we must also estimate w as a nuisance parameter. We use the ML estimation to compute

$$\hat{\theta} = \arg\max_{\theta} p_{1,\theta}(\mathbf{y}). \tag{22}$$

When we take the logarithm of $p_{1,\theta}(y)$, the above optimization is equivalent to minimizing an objective function

$$c(\mathbf{r}) = \min_{w} \|\mathbf{y} - w\mathbf{f}(\mathbf{r})\|_{\mathbf{\Upsilon}^{-1}}^2. \tag{23}$$

Setting the derivative of $\|\mathbf{y} - w\mathbf{f}(\mathbf{r})\|_{\mathbf{\Upsilon}^{-1}}$ with respect to w to zero results in the following equivalent representation of $c(\mathbf{r})$:

$$\bar{w}(\mathbf{r}) = \frac{\mathbf{f}^T(\mathbf{r})\mathbf{\Upsilon}^{-1}\mathbf{y}}{\mathbf{y}^T\mathbf{\Upsilon}^{-1}\mathbf{y}}, \tag{24}$$

$$c(\mathbf{r}) = \|\mathbf{y} - \bar{w}(\mathbf{r})\mathbf{f}(\mathbf{r})\|_{\mathbf{\Upsilon}^{-1}}^2. \tag{25}$$

We estimate the tumor position $\hat{\mathbf{r}}$ by determining the position $\mathbf{r}$ that minimizes $c(\mathbf{r})$ in Eq. (25):

$$\hat{\mathbf{r}} = \arg\min_{\mathbf{r}} c(\mathbf{r}), \tag{26}$$

$$\hat{w} = \bar{w}(\hat{\mathbf{r}}). \tag{27}$$

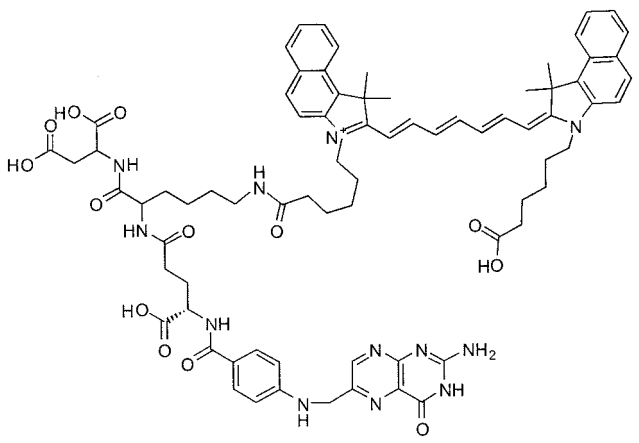

Fig. 3. Structural formula for folate-indocyanine.

With the use of closed-form Green's functions in the computation of $\mathbf{f}$, this minimization can be accomplished quickly, even when $c(\mathbf{r})$ is evaluated over an entire region of interest.

To assess the precision of our localization procedure for tumors of various depths, we compute statistical bounds on the estimator variance using a model of the measurement system. Specifically, we compute the Cramér–Rao lower bound[43] for the estimator covariance to determine a measurement's best-case performance limits. For simplicity, we neglect bias in our computations of the Cramér–Rao bound, as done previously.[26] Let $\mathbf{C} = E[(\hat{\theta} - \theta) \times (\hat{\theta} - \theta)^T]$ and let $\mathbf{J}$ be the Fisher information matrix[43] defined as $J_{mn} = E[-(\partial^2)/(\partial\theta_m \partial\theta_n)\ln p_{1,\theta}(\mathbf{y})]$. The Cramér–Rao bound requires that $\mathbf{C} \geq \mathbf{J}^{-1}$ (i.e., $\mathbf{C} - \mathbf{J}^{-1}$ is nonnegative definite). It can be shown[43] that

$$\mathbf{J} = \tilde{\mathbf{f}}'(\theta)^T \mathbf{\Upsilon}^{-1} \tilde{\mathbf{f}}'(\theta), \tag{28}$$

where

$$\tilde{\mathbf{f}}'(\theta) = \left[\frac{\partial \tilde{\mathbf{f}}(\mathbf{r})}{\partial x} \quad \frac{\partial \tilde{\mathbf{f}}(\mathbf{r})}{\partial z} \quad \frac{\partial \tilde{\mathbf{f}}(\mathbf{r})}{\partial w} \right]^T \tag{29}$$

$$= \left[w \frac{\partial \mathbf{f}(r)}{\partial x} \quad w \frac{\partial \mathbf{f}(r)}{\partial z} \quad \mathbf{f}(\mathbf{r}) \right]^T. \tag{30}$$

In Appendix A we present expressions for the required partial derivatives.

5. Experiment

A. Folate-Indocyanine, Dye Synthesis

A new folate-indocyanine dye suitable for use with 785-nm diode lasers was synthesized. The structural formula is shown in Fig. 3. We purchased 9-fluorenylmethoxy carbonyl- (Fmoc-) protected amino acid derivatives, Fmoc-aspartic acid-loaded Wang resin, 2-(1H-benzotriazol-1-yl)-1, 1, 3, 3-tetramethyluronium hexafluorophosphate (HBTU), and *N*-hydroxybenzotriazole from Novabiochem (San Diego, California). N^{10}-trifluoroacetylpteroic acid was synthesized from folic acid (Sigma Chemical Company, St. Louis, Missouri) according to a previous published report.[44] The indocyanine derivative was also synthesized according to a literature procedure.[45]

Standard Fmoc peptide chemistry was used to synthesize a folate peptide linked to indocyanine attached to the gamma carboxy of folic acid. The sequence Asp-Lys-(γ)Glu-pteroic acid was constructed by Fmoc chemistry with HBTU and *N*-hydroxybenzotriazole as the activating agents, along with diisopropyethylamine as the base and 20% piperidine in dimethylformamide for deprotection of the Fmoc groups. Fmoc-protected lysine containing a 4-methyltrityl protecting group on the ε-amine was linked to Fmoc-protected glycine attached to a Wang resin. An α-t-Boc protected N-α-Fmoc glutamic acid was then linked to the peptide to provide a γ-linked conjugate on folate after attaching N^{10}-trifluoroacetylpteroic acid to the peptide. The methoxytrityl protecting group on the ε-amine of lysine was removed with 1% trifluoroacetic acid in dichloromethane to allow attachment of indocyanine. Indocyanine, diisopropylethylamine, and activating agents (added slowly to the indocyanine solution) were reacted overnight with the peptide and then washed thoroughly from the peptide resin beads. The folate-indocyanine peptide was then cleaved from the resin with 95% trifluoroacetic acid:2.5% water:2.5% triisopropylsilane solution. Diethyl ether was used to precipitate the product, and the precipitant was collected by centrifugation. The product was then washed twice with diethyl ether and dried under vacuum overnight. To remove the N^{10}-trifluoracetyl protecting group, the product was dissolved in 5 ml of water containing 0.5 ml of 10% ammonium hydroxide and stirred for 30 min at room temperature. The sample was then precipitated with isopropanol and ether; the precipitant was collected by centrifugation and then added to a G-10 Sephadex gel filtration column (1.5 cm × 15 cm) with water as the eluent. The product peaks were collected and lyophilized.

B. Animal Studies

To demonstrate the effect of the folate-indocyanine dye, we acquired images of a fluorescing tumor on a mouse subject. All animal procedures were carried out with approval from the Purdue Animal Care and Use Committee. Nu/nu mice were purchased from Harlan (Indianapolis, Indiana). The mice were at least eight weeks old when purchased and were immediately placed on folate-deficient chow (Harlan, Indianapolis, Indiana); this occurred at least two weeks prior to imaging. Tumors were induced into the mice by injection of approximately 500,000 L1210 cells subcutaneously. Imaging was performed approximately two weeks after tumor induction or when tumors reached approximately 1 cm in diameter.

We injected the folate-indocyanine conjugate into

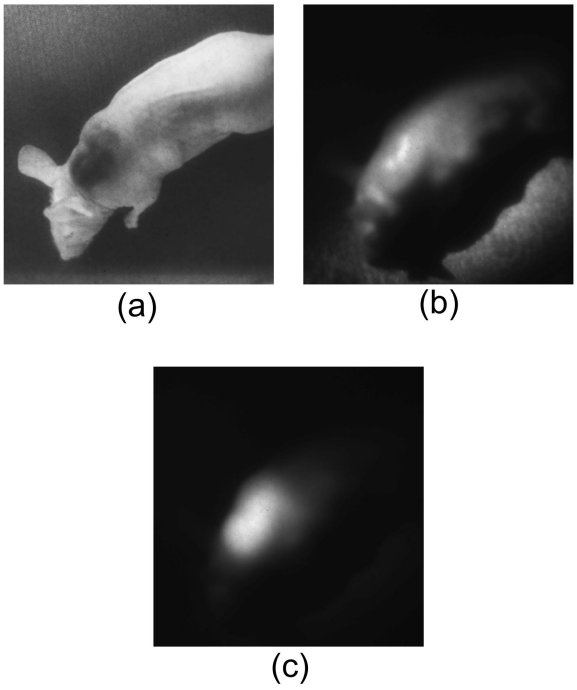

Fig. 4. Nu/nu mouse injected with folate-indocyanine, which selectively targets FRs on the tumors. The illumination is due to (a) room light, (b) 785-nm excitation, (c) 820-nm emission.

the femoral vein of the mice by making an incision in the leg to expose the vein. We then injected 100 μl of a phosphate-buffered saline solution containing 20 μg of the folate dye conjugate and images were collected 2 h later. The wound was closed with Vetbond (The Butler Co., Indianapolis, Indiana), and the mice were euthanized prior to imaging.

Figure 4 shows images of a nu/nu mouse with a L1210 tumor. The mouse was illuminated under an expanded laser diode beam at 785 nm, and images were acquired with a Roper PI-MAX intensified CCD camera. For the fluorescence measurements, a bandpass filter in the 820-nm range with 10 nm FWHM was placed over the camera. Figure 4(b) shows an image at the 785-nm laser excitation, and Fig. 4(c) shows the fluorescence emitted from the mouse. From these images, it is clear that the dye provides high contrast between tumors and the surrounding tissue. In other experiments, we have shown that the dye results in significantly increased fluorescence compared with nontargeted indocyanine controls, but we omit these results here for brevity.

C. Tumor Localization Measurement

Figure 5 schematically depicts an experiment to localize a fluorescent mouse tumor submerged under a lipid suspension. A nu/nu mouse was induced to grow a lung tumor, injected intravenously with folate-indocyanine, and euthanized as described in Subsection 5.B. The tumor was excised and cut into two fragments. Each of the two tumor fragments was glued (with Vetbond) to the bottom of a cylindrical, 8.6-cm-diameter, 1.8-cm-deep plastic Petri dish.

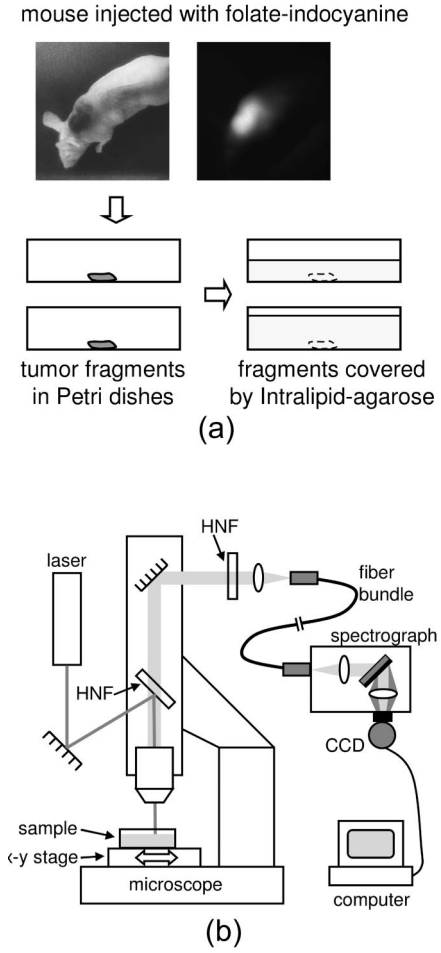

Fig. 5. Schematic depictions of tumor localization experiment. (a) A tumor-bearing mouse is injected with folate-indocyanine and the excised tumor fragments are bonded to Petri dishes and covered with Intralipid and agarose. (b) The sample is scanned in a near-IR fluorescence microscope and measurements are recorded. HNF, holographic notch filter.

Each tumor fragment was approximately 5 mm in diameter and no thicker than 2 mm. The Petri dishes were then filled with a solid gel phantom, prepared from a suspension of 1% Intralipid and agarose.[46] In the 800-nm light wavelength range, 1% Intralipid has $\mu_a = 0.030\ \mathrm{cm}^{-1}$ and $D = 0.033$ cm,[47,48] similar to the scatter of human tissue. The absorption of this suspension is lower than that of human tissue, although μ_a has previously been measured at around $0.040–0.050\ \mathrm{cm}^{-1}$ in certain tissue types for this wavelength range.[30] One of the Petri dishes was filled to a height of 0.79 cm, and the other was filled to a height of 1.20 cm. Assuming that the tumor centers were approximately 0.1 cm from the bottom of the Petri dishes, the true tumor depths were taken to be 0.69 and 1.1 cm.

To perform the fluorescence scan measurement, a previously described near-IR Raman imaging microscope system[49,50] was used. This system was originally designed for fast Raman spectral imaging by use of a 2-D square fiber bundle, a spectrograph, and

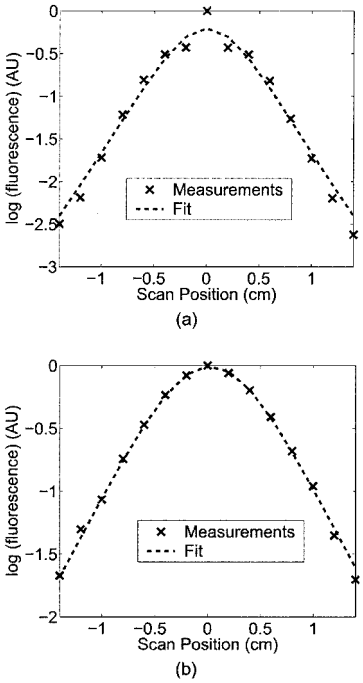

Fig. 6. Normalized mouse tumor fluorescence intensity scans for two different Intralipid depths: (a) 0.69 cm deep and (b) 1.1 cm deep. The dashed curves show the best fit to a diffusion model with a point fluorophore.

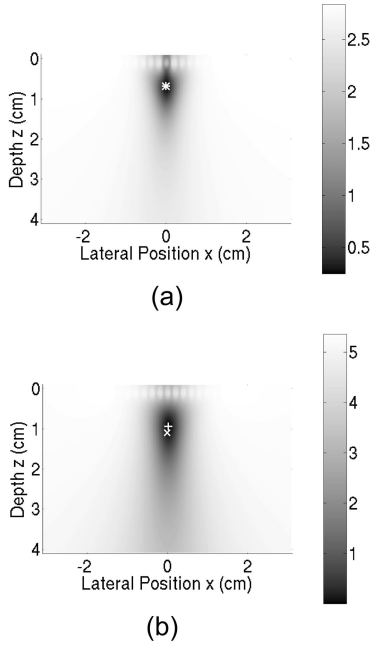

Fig. 7. Cost function versus tumor position for a mouse tumor obscured under (a) 0.69 cm and (b) 1.1 cm of Intralipid. The × symbol marks the true tumor location; the + symbol marks the estimated location.

a CCD detector. Rather than collecting a 2-D spatial grid of spectral data, we used the system to collect only a single fluorescence spectrum for each sample position. A diode laser (SDL-8630) operating at 785 nm was fiber coupled into a microscope, illuminating the sample from above with ≈100 mW of power. The same microscope simultaneously collected the fluorescence migrating from the obscured tumor to the top of the sample. The spectra were recorded by use of a spectrograph and a CCD detector (Princeton Instruments LN/CCD-1024 EHRB). The sample was moved in one dimension with a motorized translation stage to 15 different positions, at a spacing of 0.2 cm, with the middle measurement position directly above the tumor. To minimize noise in our measurements, integration times of 20 s were used (although the emission could be clearly observed for shorter integration times). For each sample, a background spectrum was recorded over the Intralipid far from the tumor position. This measurement was used to subtract any effects due to dark current or background signal from the tumor fluorescence signal.

For each recorded spectrum, we formed an intensity measurement by integrating over wavelengths from 800 to 840 nm. The resulting intensity measurement scans for both samples, with each scan normalized to arbitrary units, are shown in Fig. 6. The localization procedure described in Eq. (27) was used to estimate the tumor's location, and the resulting best-fit diffusion model computations are plotted in Fig. 6 for comparison purposes. The surface plots of Fig. 7 show $c(\mathbf{r})$ in the vertical plane of points directly underneath the measurement scan computed for each of the two phantoms. The tumor coordinates were estimated to be at $(x, z) = (0.00, 0.68)$ cm and $(x, z) = (0.02, 0.95)$ cm, compared with the corresponding true coordinates $(x, z) = (0.00, 0.69)$ cm and $(x, z) = (0.00, 1.1)$ cm.

To compute the results of Fig. 7, we used $[\mathbf{Y}]_{ii} = |y_i|$, rather than Eq. (8), because α was unknown. This results in an unknown scalar factor for the cost function $c(\mathbf{r})$, which has no effect on the optimization in Eq. (27). We address the question of determining α in Subsection 5.D.

D. Detection and Localization Performance Bounds

To assess the diagnostic capabilities of the detection and localization methods, we considered the question of how deeply a realistic tumor could be embedded but still detected with high probability and localized with good precision. Because of the geometric constraints imposed by the microscope, we were unable to measure Intralipid–agarose samples substantially thicker than the ones described in Subsection 5.C. Hence we computed theoretical performance bounds using the methods of Section 3 and Subsection 4.A. To develop a model for the measurement system, it was necessary to determine the noise scaling parameter α. From the data and fit depicted in Fig. 6(b), we computed the ML estimate of α as[41]

$$\hat{\alpha} = \frac{1}{P} \left\| \mathbf{y} - \hat{w}\mathbf{f}(\hat{\mathbf{r}}) \right\|^2_{\tilde{\mathbf{Y}}^{-1}}, \tag{31}$$

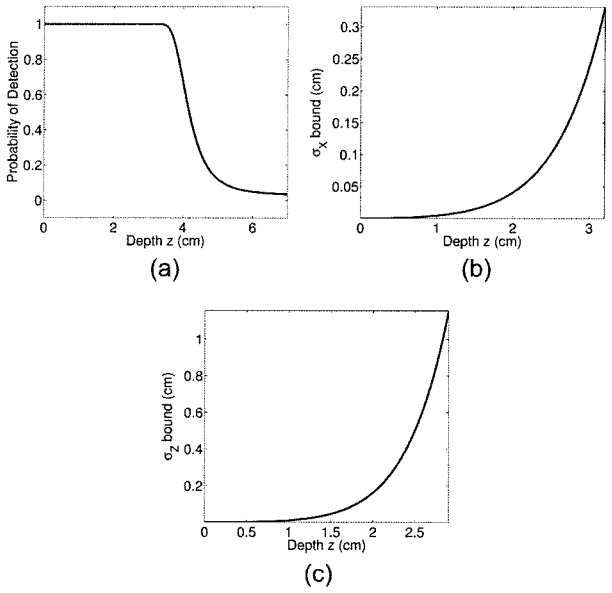

Fig. 8. Theoretical performance bounds for tumor measurement as a function of tumor depth. (a) Probability of detection for a false-alarm rate of 0.03. (b) Cramér–Rao bound for σ_X. (c) Cramér–Rao bound for σ_Z.

where $[\tilde{\Upsilon}]_{ii} = |y_i|$ and P is the number of measurements.

Using the models in Section 2, we obtained bounds on the tumor detection probability and on the tumor localization error as described in Section 3 and Subsection 4.A. To compute the probability of detection and the Cramér–Rao bounds as a function of tumor position $\mathbf{r}$ for a realistic tumor, we used $\mathbf{\Upsilon} = \hat{\alpha}\hat{w}\ \mathrm{diag}|f(\mathbf{r})|$, where $\hat{w}$ was the estimate obtained in Subsection 5.C with the data of Fig. 6. This shot-noise model is similar to the one described in Eq. (8), but with y_i replaced by its expected value $\hat{w}f_i(\mathbf{r})$. Figure 8(a) shows the probability of tumor detection as a function of z, for a false alarm rate of 0.03, computed with Eq. (21). This plot is an idealization because of the model simplifications described in Subsection 2.B and because the ROC is based on the LRT rather than the GLRT. Nevertheless, it provides useful best-case information and shows that it is difficult to detect a tumor deeper than approximately 3.5 cm [the cutoff in Fig. 8(a)] with this measurement device. Figures 8(b) and 8(c) show lower bounds on the standard deviations σ_X and σ_Z of the position estimates of x and z, respectively, computed with Eq. (28). The assumption of a point-source representation is considered to be valid for all positions in this example.

6. Conclusion

We have presented an approach for detecting and localizing an obscured, fluorescing tumor, using a statistical framework. We use this framework to compute the probability of tumor detection and tumor localization precision bounds. We considered a 1-D measurement scan, with the excitation and collection at the same location above the sample. The method could be extended to 2-D planar measurement geometries for 3-D localization. In principle, a similar geometry could be employed in the clinic in the form of a scanning fluorescence probe that is waved over a tissue region, or a small probe placed on a tissue surface. Such measurements could facilitate intraoperative detection and localization of tumors, allowing a surgeon to remove all tumors while minimizing damage to surrounding tissue.

The measurement system used to perform the experiment was not originally designed for this application, and several improvements could be made in subsequent research. The near-IR Raman imaging microscope system used in the experiment collects emitted light from an area that is of the order of 1 μm in diameter.[49] A larger-aperture detection system could be used to reduce the exposure times. Time- or frequency-domain measurements, rather than only cw measurements, would potentially provide additional detection and localization criteria that are useful. In addition, all the methods and analyses presented here can be extended to more sophisticated, multiple source–detector geometries that are typically used in FODT. Another possibility is that the approach of dual interfering sources[51,3] studied for 2-D tumor localization could be combined with our approach for estimating tumor depth, potentially resulting in a more accurate 3-D localization. An important future step would be to apply our analysis methods to *in vivo* tumor detection and localization. The excising of the mouse tumor and measurement in an Intralipid–agarose suspension provided a carefully controlled experiment for our initial studies. For *in vivo* experiments, irregular surfaces and possibly inhomogeneous tissue properties might have to be addressed.[52]

The fast detection and localization approach presented here could serve as a real-time complement to more computationally demanding, but more quantitative, FODT reconstruction algorithms. In addition, detection and localization of a fluorescing tumor might provide useful prior knowledge that can be incorporated into Bayesian FODT reconstruction approaches.[3] The ROC and the Cramér–Rao bound results presented here could also be used to optimize a FODT measurement system geometry for the tasks of detection and localization. These possibilities, combined with the high tumor-to-background contrast offered by the folate-indocyanine imaging agent, could improve the performance in fluorescence-enhanced optical mammography[53] or other diagnostic imaging applications.

Appendix A: Partial Derivatives for the Cramér–Rao Bound

Here we compute the partial derivatives required in Eq. (28). We first rewrite $f_i(\mathbf{r})$:

$$f_i(\mathbf{r}) = [a_i(\mathbf{r}) - b_i(\mathbf{r})^2, \tag{A1}$$

where a_i and b_i are the first and second terms in the

brackets of Eq. (6), respectively. The partial derivatives are as follows:

$$\frac{\partial f_i}{\partial x} = 2(a_i - b_i)\left(\frac{\partial a_i}{\partial x} - \frac{\partial b_i}{\partial x}\right), \tag{A2}$$

$$\frac{\partial f_i}{\partial z} = 2(a_i - b_i)\left(\frac{\partial a_i}{\partial z} - \frac{\partial b_i}{\partial z}\right), \tag{A3}$$

$$\frac{\partial a_i}{\partial x} = -(x - x_{s_i})a_i({r_a}^{-2} + k{r_a}^{-1}), \tag{A4}$$

$$\frac{\partial a_i}{\partial z} = -(z - z_{s_i})a_i({r_a}^{-2} + k{r_a}^{-1}), \tag{A5}$$

$$\frac{\partial b_i}{\partial x} = -(x - x_{s_i})b_i({r_b}^{-2} + k{r_b}^{-1}), \tag{A6}$$

$$\frac{\partial b_i}{\partial z} = -(z + z_{s_i} + 2l_s)b_i({r_b}^{-2} + k{r_b}^{-1}). \tag{A7}$$

This research was funded by the National Science Foundation under contract CCR-0073357. We gratefully acknowledge Hartmut G. Hedderich and Dor Ben-Amotz for their assistance in the laboratory experiment.

Send correspondence regarding this paper to Kevin J. Webb, School of Electrical and Computer Engineering, Purdue University, 465 Northwestern Avenue, West Lafayette, Indiana 47907-2035. E-mail, webb@purdue.edu.

References

1. W. Jager, H. Feistel, E. M. Paterok, G. Ronay, A. H. Tulusan, F. Wolf, and N. Lang, "Resection guided by antibodies (REGAJ): a diagnostic procedure during second-look operation in ovarian cancer patients," Br. J. Cancer Suppl. **10,** 18–20 (1990).
2. V. Ntziachristos, C. Bremer, and R. Weissleder, "Fluorescence imaging with near-infrared light," Eur. Radiol. **13,** 195–208 (2003).
3. A. B. Milstein, J. J. Stott, S. Oh, D. A. Boas, R. P. Millane, C. A. Bouman, and K. J. Webb, "Fluorescence optical diffusion tomography using multiple-frequency data," J. Opt. Soc. Am. A **21,** 1035–1049 (2004).
4. A. B. Milstein, S. Oh, K. J. Webb, C. A. Bouman, Q. Zhang, D. A. Boas, and R. P. Millane, "Fluorescence optical diffusion tomography," Appl. Opt. **42,** 3081–3094 (2003).
5. R. Roy and E. M. Sevick-Muraca, "Three-dimensional unconstrained and constrained image-reconstruction techniques applied to fluorescence, frequency-domain photon migration," Appl. Opt. **40,** 2206–2215 (2001).
6. M. A. O'Leary, D. A. Boas, X. D. Li, B. Chance, and A. G. Yodh, "Fluorescence lifetime imaging in turbid media," Opt. Lett. **21,** 158–160 (1996).
7. J. Chang, H. L. Graber, and R. L. Barbour, "Luminescence optical tomography of dense scattering media," J. Opt. Soc. Am. A **14,** 288–299 (1997).
8. V. Ntziachristos and R. Weissleder, "Experimental three-dimensional fluorescence reconstruction of diffuse media by use of a normalized Born approximation," Opt. Lett. **26,** 893–895 (2001).
9. E. Shives, Y. Xu, and H. Jiang, "Fluorescence lifetime tomography of turbid media based on an oxygen-sensitive dye," Opt. Express **10,** 1557–1562 (2002), www.opticsexpress.org.
10. Y. Chen, G. Zheng, Z. H. Zhang, D. Blessington, M. Zhang, H. Li, Q. Liu, L. Zhou, X. Intes, S. Achilefu, and B. Chance, "Metabolism-enhanced tumor localization by fluorescence imaging: *in vivo* animal studies," Opt. Lett. **28,** 2070–2072 (2003).
11. I. Gannot, A. Garashi, G. Gannot, V. Chernomordik, and A. Gandjbakhche, "*In vivo* quantitative three-dimensional localization of tumor labeled with exogenous specific fluorescence markers," Appl. Opt. **42,** 3073–3080 (2003).
12. E. L. Hull, M. G. Nichols, and T. H. Foster, "Localization of luminescent inhomogeneities in turbid media with spatially resolved measurements of cw diffuse luminescent emittance," Appl. Opt. **37,** 2755–2765 (1998).
13. M. Pfister and B. Scholz, "Localization of fluorescent spots with space-space MUSIC for mammographylike measurement system," J. Biomed. Opt. **9,** 481–487 (2004).
14. G. Toffoli, C. Cernigoi, A. Russo, A. Gallo, M. Bagnoli, and M. Boiocchi, "Overexpression of folate binding protein in ovarian cancers," Int. J. Cancer **74,** 193–198 (1997).
15. P. Garin-Chesa, I. Campbell, P. E. Saigo, J. L. Lewis, Jr., L. J. Old, and W. J. Rettig, "Trophoblast and ovarian cancer antigen LK26. Sensitivity and specificity in immunopathology and molecular identification as a folate-binding protein," Am. J. Pathol. **142,** 557–567 (1993).
16. T. A. Patrick, D. M. Kranz, T. A. van Dyke, and E. Roy, "Folate receptors as potential therapeutic targets in choroid plexus tumors of SV40 transgenic mice," J. Neuro-Oncol. **32,** 111–123 (1997).
17. W. J. Rettig, C. Cordon-Cardo, J. P. Koulos, J. L. Lewis, H. F. Oettgen, and L. J. Old, "Cell surface antigens of human trophoblast and choriocarcinoma defined by monoclonal antibodies," Int. J. Cancer **35,** 469–475 (1985).
18. W. A. Franklin, M. Waintrub, D. Edwards, K. Christensen, P. Prendegrast, J. Woods, P. A. Bunn, and J. F. Kolhouse, "New anti-lung-cancer antibody cluster 12 reacts with human folate receptors present on adenocarcinoma," Int. J. Cancer Suppl. **8,** 89–95 (1994).
19. J. Selhub and W. A. Franklin, "The folate-binding protein of rat kidney. Purification, properties, and cellular distribution," J. Biol. Chem. **259,** 6601–6606 (1984).
20. M. D. Kennedy, K. Jallad, J. Lu, P. S. Low, and D. Ben-Amotz, "Evaluation of folate conjugate uptake and transport by the choroid plexus of mice," Pharm. Res. **20,** 714–719 (2003).
21. S. D. Weitman, K. M. Frazier, and B. A. Kamen, "The folate receptor in central nervous system malignancies of childhood," J. Neuro-Oncol. **21,** 107–112 (1994).
22. C. J. Mathias, S. Wang, R. J. Lee, D. J. Waters, P. S. Low, and M. A. Green, "Tumor-selective radiopharmaceutical targeting via receptor-mediated endocytosis of gallium-67-deferoxamine-folate," J. Nucl. Med. **37,** 1003–1008 (1996).
23. S. D. Konda, M. Aref, M. Brechbiel, and E. C. Wiener, "Development of a tumor-targeting MR contrast agent using the high-affinity folate receptor: work in progress," Invest. Radiol. **35,** 50–57 (2000).
24. M. D. Kennedy, K. N. Jallad, D. H. Thompson, D. Ben-Amotz, and P. S. Low, "Optical imaging of metastatic tumors using a folate-targeted fluorescent probe," J. Biomed. Opt. **8,** 636–641 (2003).
25. C.-H. Tung, Y. Lin, W. K. Moon, and R. Weissleder, "A receptor-targeted near-infrared fluorescence probe for *in vivo* tumor imaging," ChemBioChem **3,** 784–786 (2002).
26. A. J. Devaney and G. A. Tsihrintzis, "Maximum likelihood estimation of object location in diffraction tomography," IEEE Trans. Signal Process. **39,** 672–682 (1991).
27. J. C. Ye, Y. Bresler, and P. Moulin, "Cramér–Rao bounds for

2-D target shape estimation in nonlinear inverse scattering problems with application to passive radar," IEEE Trans. Antennas Propag. **49,** 771–783 (2001).
28. G. Boverman, "Modeling and nonlinear inversion for frequency domain diffuse optical tomography," Master's thesis (Northeastern University, Boston, Mass., 2003).
29. E. L. Miller and A. S. Willsky, "Multiscale, statistical anomaly detection analysis and algorithms for linearized inverse scattering problems," Multidimens. Syst. Signal Process. **8,** 151–184 (1995).
30. A. Torricelli, A. Pifferi, P. Taroni, E. Giambattistelli, and R. Cubeddu, "*In vivo* optical characterization of human tissues from 610 to 1010 nm by time-resolved reflectance spectroscopy," Phys. Med. Biol. **46,** 2227–2237 (2001).
31. R. M. P. Doornbos, R. Lang, M. C. Aalders, F. W. Cross, and H. J. C. M. Sterenborg, "The determination of *in vivo* human tissue optical properties and absolute chromophore concentrations using spatially resolved steady-state diffuse reflectance spectroscopy," Phys. Med. Biol. **44,** 967–981 (1999).
32. S. Chandrasekhar, *Radiative Transfer* (Dover, New York, 1960).
33. J. J. Duderstadt and L. J. Hamilton, *Nuclear Reactor Analysis* (Wiley, New York, 1976).
34. M. S. Patterson and B. W. Pogue, "Mathematical model for time-resolved and frequency-domain fluorescence spectroscopy in biological tissues," Appl. Opt. **33,** 1963–1974 (1994).
35. E. M. Sevick-Muraca, G. Lopez, J. S. Reynolds, T. L. Troy, and C. L. Hutchinson, "Fluorescence and absorption contrast mechanisms for biomedical optical imaging using frequency-domain techniques," Photochem. Photobiol. **66,** 55–64 (1997).
36. J. S. Reynolds, C. A. Thompson, K. J. Webb, F. P. LaPlant, and D. Ben-Amotz, "Frequency domain modeling of reradiation in highly scattering media," Appl. Opt. **36,** 2252–2259 (1997).
37. A. Ishimaru, *Wave Propagation and Scattering in Random Media* (Academic, New York, 1978), Vol. 1.
38. R. C. Haskell, L. O. Svaasand, T.-T. Tsay, T.-C. Feng, M. S. McAdams, and B. J. Tromberg, "Boundary conditions for the diffusion equation in radiative transfer," J. Opt. Soc. Am. A **11,** 2727–2741 (1994).
39. K. J. Webb, A. B. Milstein, M. D. Kennedy, K. N. Jallad, C. A. Bouman, D. Ben-Amotz, and P. S. Low, "Folate conjugate fluorescence labeling for tumor localization," in *Third Inter-Institute Workshop on Diagnostic Optical Imaging and Spectroscopy: The Clinical Adventure* (National Institutes of Health, Bethesda, Md., 2002).
40. J. C. Ye, K. J. Webb, C. A. Bouman, and R. P. Millane, "Optical diffusion tomography using iterative coordinate descent optimization in a Bayesian framework," J. Opt. Soc. Am. A **16,** 2400–2412 (1999).
41. J. C. Ye, C. A. Bouman, K. J. Webb, and R. P. Millane, "Nonlinear multigrid algorithms for Bayesian optical diffusion tomography," IEEE Trans. Image Process. **10,** 909–922 (2001).
42. H. L. van Trees, *Detection, Estimation, and Modulation Theory* (Wiley, New York, 1968), Part I.
43. L. L. Scharf, *Statistical Signal Processing: Detection, Estimation, and Time Series Analysis* (Addison-Wesley, New York, 1990).
44. J. Luo, M. Smith, D. A. Lantrip, S. Wang, and P. L. Fuchs, "Efficient synthesis of pyrofolic acid and pteroyl A azide, reagents for the production of carboxyl differentiated derivatives of folic acid," J. Am. Chem. Soc. **119,** 10004–10013 (1997).
45. S. Achilefu, R. Dorshow, J. Bugaj, and R. Rajagopalan, "Novel receptor-targeted fluorescent contrast agents for *in vivo* tumor imaging," Invest. Radiol. **35,** 479–485 (2000).
46. G. Wagnières, S. Cheng, M. Zellweger, N. Utke, D. Braichotte, J. Ballini, and H. van der Bergh, "An optical phantom with tissue-like properties in the visible for use in PDT and fluorescence spectroscopy," Phys. Med. Biol. **42,** 1415–1426 (1997).
47. G. M. Hale and M. R. Querry, "Optical constants of water in the 200-nm to 200-μm wavelength region," Appl. Opt. **12,** 555–563 (1973).
48. H. J. van Staveren, C. J. M. Moes, J. van Marie, S. A. Prahl, and M. J. C. van Gemert, "Light scattering in Intralipid-10% in the wavelength range of 400–1100 nm," Appl. Opt. **30,** 4507–4514 (1991).
49. A. D. Gift, J. Ma, K. S. Haber, B. L. McClain, and D. Ben-Amotz, "Near-infrared Raman imaging microscope based on fiber-bundle image compression," J. Raman Spectrosc. **30,** 757–765 (1999).
50. B. L. McClain, H. G. Hedderich, A. D. Gift, D. Zhang, K. N. Jallad, K. S. Haber, J. Ma, and D. Ben-Amotz, "Fast chemical imaging: a rapid, noninvasive tool for medical, materials, and process analyses," Spectroscopy **15,** 28–37 (2000).
51. M. G. Erickson, J. S. Reynolds, and K. J. Webb, "Comparison of sensitivity for single and dual interfering source configurations in optical diffusion imaging," J. Opt. Soc. Am. A **14,** 3083–3092 (1997).
52. R. B. Schulz, J. Ripoll, and V. Ntziachristos, "Experimental fluorescence tomography of tissues with noncontact measurements," IEEE Trans. Med. Imaging **23,** 492–500 (2004).
53. V. Ntziachristos, A. G. Yodh, M. Schnall, and B. Chance, "Concurrent MRI and diffuse optical tomography of breast after indocyanine green enhancement," Proc. Natl. Acad. Sci. USA **97,** 2767–2772 (2000).